PLANETESIMAL ACCRETION AT SHORT ORBITAL PERIODS

Spencer C. Wallace[1] and Thomas R. Quinn[1]

[1]*Astronomy Department, University of Washington, Seattle, WA 98195*

ABSTRACT

Formation models in which terrestrial bodies grow via the pairwise accretion of planetesimals have been reasonably successful at reproducing the general properties of the solar system, including small body populations. However, planetesimal accretion has not yet been fully explored in the context of more exotic terrestrial systems, particularly those that host short-period planets. In this work, we use direct N-body simulations to explore and understand the growth of planetary embryos from planetesimals in disks extending down to $\simeq 1$ day orbital periods. We show that planetesimal accretion becomes nearly 100 percent efficient at short orbital periods, leading to embryo masses that are roughly twice as large as the classical isolation mass. For rocky bodies, the physical size of the object begins to occupy a significant fraction of its Hill sphere at orbital periods less than about 50 days. In this regime, most close encounters result in collisions, rather than scattering, and the system cannot bifurcate into a collection of dynamically hot planetesimals and dynamically cold oligarchs, like is seen in previous work. The highly efficient accretion seen at short orbital periods implies that systems of tightly-packed inner planets should be almost completely devoid of any residual small bodies. We demonstrate the robustness of our results to assumptions about the initial disk model, and also investigate how far material can radially mix across the boundary between modes.

1. INTRODUCTION

Planetesimal accretion is a key phase in the terrestrial planet growth process, bridging the gap from kilometer-sized bodies up to roughly moon-sized objects known as planetary embryos. In the earliest stages of the planet formation process, aerodynamic forces dominate the growth and evolution of the solids and statistical models (Johansen et al. 2014; Birnstiel et al. 2016) are appropriate to describe how these numerous, small bodies coagulate. Due to the internal pressure support of the gas disk, the gas itself orbits at sub-Keplerian speed and exerts a headwind on any solids large enough to decouple from the gas (Weidenschilling 1977). Above about a meter in size, this headwind is maximally effective at sapping away angular momentum, and planet-building material can fall onto the central star on catastrophically short timescales (Weidenschilling 1977; Nakagawa et al. 1986). Additionally, laboratory experiments suggest that collisions between mm- to cm- sized solids tend to result in bouncing or destruction, rather than continued growth (Blum & Münch 1993; Beitz et al. 2011; Colwell 2003). For these reasons, a number of mechanisms which involve radially concentrating solids in a planet-forming disk have been proposed to facilitate fast growth from mm to km sizes (Johansen et al. 2007; Lyra et al. 2008; Bai & Stone 2010). Interestingly, formation models for the short-period multiplanet systems revealed by Kepler (Fabrycky et al. 2014) also seem to require enhanced concentrations of planet-building material to reproduce the observed architectures (Raymond et al. 2007; Hansen & Murray 2012).

Regardless of how the mm- to km-sized growth barriers are surmounted, gravity begins to dominate and aerodynamic gas drag plays a less significant role beyond this size. During this phase, collision cross sections are enhanced as gravitational focusing (Safronov 1969) acts to bend the trajectories of bodies undergoing close encounters. Because larger bodies are more effective at focusing the trajectories of nearby planetesimals, a period of runaway growth occurs (Wetherill & Stewart 1989; Kokubo & Ida 1996; Barnes et al. 2009). Eventually, the largest bodies (known as oligarchs) dynamically heat the surrounding planetesimals, severely limiting further growth (Kokubo & Ida 1998). The end result of this phase is a bimodal population of dynamically cold oligarchs, surrounded by dynamically hot, difficult to accrete residual planetesimals. Lines of evidence suggest that the asteroid belt, Kuiper belt and the Oort cloud are largely composed of the leftovers of this stage of planet formation.

After a long period of quiescence, the collection of embryos and remaining planetesimals undergoes a large-scale instability (Chambers & Wetherill 1998). As a consequence of the instability, the oligarchics are no longer on isolated, stable orbits and coalesce to form Earth-

sized planets' through a series of extremely energetic, giant impacts (Kokubo & Ida 2002; Raymond et al. 2005, 2006).

Due to the relative ease of modeling the early dust coagulation phases and the final giant impact phase, these steps in the terrestrial planet formation process have received the most attention in the literature. The planetesimal accretion phase, which we will focus on in this paper, falls into an awkward in-between, where there are too many particles to directly track with traditional N-body codes, while the gravitational influence of the few, but massive oligarchs that form make statistical methods an inappropriate approach. Because of this limitation, planetesimal accretion is usually modeled in a narrow ring, and the results are then scaled to suit whatever situation is being studied. N-body simulations of terrestrial planet formation typically begin with a series of neatly spaced oligarchs, whose mass varies smoothly with orbital period. As we will show in this paper, this extrapolation with orbital period is inappropriate, particularly at short (< 10 day) periods.

Given that systems of tightly-packed inner planets (STIPs) appear to be a common outcome of planet formation, understanding exactly how solids accumulate at short orbital periods is crucial. Although gas-disk driven migration of the planets themselves is often invoked to explain the observed architectures, we will focus on an in-situ model in this paper. That is, once the planetesimals themselves form, they largely stay in place and any subsequent large-scale movement of the solids are the result of mutual gravitational interactions. The focus of this work will be to understand how the outcome of the planetesimal accretion process scales with orbital period by using a high-powered N-body code to directly follow the growth and evolution of the planetesimals across a wide range of orbital periods (1 to 100 days). In doing so, we will assess whether the typical "isolation mass" initial conditions used in studies of terrestrial planet formation are actually appropriate for understanding STIPs. In a series of follow up papers, we plan to use these results to directly track the formation of full-sized planets from planetesimals and to understand how gravitational perturbations from a nearby gas giant might affect the outcome of this process.

In section 2 we provide an overview of the theory behind planetesimal accretion and show that assumptions used to derive the well-known modes of growth are only valid at sufficiently long orbital periods. We then motivate the need for N-body simulations to study this problem and describe the code used, along with how our initial conditions were constructed in section 3. In section 4, we present a parameter study of planetesimal accretion using a series of simulations of narrow annuli at various orbital periods. In section 5 we present a set of simulations starting with a much wider planetesimal disk and demonstrate that a transition between accretion modes occurs at moderately small ($\simeq 50$d) orbital periods. Next, we assess the impact of simplifications made to our collision model on this result in section 6. In section 7, we discuss the implications of this multi-modal accretion behavior throughout the disk for planet formation models and conclude.

2. OVERVIEW OF PLANETESIMAL ACCRETION
2.1. *Oligarchic and Runaway Growth*

We begin our analysis by considering a disk of equal planetesimals with radius r_{pl}, mass m_{pl} and surface density Σ_{pl}. The collision rate in the vicinity of an orbit defined by Keplerian frequency Ω can be written as $n\Gamma v$, where $n = \Sigma_{pl}\Omega/2m_{pl}v$ (where we have assumed that the scale height of the planetesimal disk goes as $\Omega/(2v)$. Γ describes the effective collision cross section and v is the typical encounter velocity between planetesimals. For a swarm of planetesimals on randomly oriented orbits, v is typically taken to the rms velocity, which can be related to the eccentricity and inclination distribution (e, i) in the following way (Lissauer & Stewart 1993):

$$\langle v^2 \rangle^{1/2} = \left(\frac{5}{4} \langle e^2 \rangle^{1/2} + \langle i^2 \rangle^{1/2} \right) v_k. \qquad (1)$$

Assuming that every collision results in a perfect merger, the growth rate of a planetesimal is given by

$$\frac{dM}{dt} = \frac{\Sigma\Omega}{2m_{pl}}\Gamma. \qquad (2)$$

In the case where the collision cross section, depends only on the physical size of the planetesimals, the growth scales linearly with mass and the mass distribution is expected to evolve in an "orderly" fashion. However, bodies larger than ~ 100 km in size are expected to exert a significant gravitational force on each other during encounters and the collision cross section depends on both the size of the bodies and their encounter velocities. In this case, $\Gamma = \Gamma_{geo}\left(1 + v_{esc}^2/v^2\right)$ (Safronov 1969), where v_{esc} is the escape velocity from the two bodies at the point of contact.

In the limit that $v_{esc} \gg v$, it can be shown that $\dot{M} \propto M^{4/3}$, which implies a runaway scenario, in which growth accelerates with mass. This mode of growth was confirmed with N-body simulations by Kokubo & Ida (1996) and appears necessary to construct protoplanets within the lifetime of a protoplanetary disk. Due to the velocity dependence of the gravitational focusing effect, it is not clear how ubiquitous this mode of growth is. In

particular, encounter velocities at short orbital periods will be rather large (because $v \sim v_k$) and the $v_{esc} \gg v$ condition may not always be satisfied. The effect that a dynamically hot disk has on runway growth will be examined in detail in section 4.

An important feature is missing from the model described above, which limits its applicability at late times. Encounters between planetesimals that do not result in a collision play a crucial role over long timescales. These close encounters act to convert energy from Keplerian shear into random motion. Over time, this gravitational stirring effect will raise the typical encounter velocities between bodies and diminish the effectiveness of gravitational focusing. With a spectrum of masses, these velocity differences become even more pronounced because as the system evolves, it moves to a state of energy equipartition where $v \sim m^{1/2}$. For a system of equal mass bodies in which encounters are driven by random motions rather than Keplerian shear (dispersion dominated), the timescale for gravitational stirring is described by the two-body relaxation time (Ida & Makino 1993)

$$t_{relax} = \frac{v^3}{4\pi n G^2 m_{pl}{}^2 \ln \Lambda}, \qquad (3)$$

where $\ln \Lambda$ is the Coulomb logarithm, typically taken to be ≈ 10 for a planetesimal disk. Despite the fact that the behavior of gravitational stirring is well-described by the two-body formalism, (Ida & Makino 1993) found that the stirring in a planetesimal disk is actually driven by close encounters. As we will show in section 4, gravitational stirring effectively shuts off when the Hill sphere of a body becomes comparable to its physical size. In this case, close encounters tend to result in collisions, and the main pathway for energy exchange between planetesimals is unable to operate.

As mentioned above, the system will tend toward a state of energy equipartition for a non-uniform mass distribution. Kokubo & Ida (1998) showed that runaway growth is actually self-limiting. As the runaway bodies grow larger, they become more effective at heating the remaining planetesimals, which diminishes the effectiveness of gravitational focusing and throttles the growth rate. Around the time that the mass of the runaway bodies exceeds the mass of the planetesimals by a factor of $\sim 50 - 100$ (depending on the orbital period) (Ida & Makino 1993) a phase of less vigorous "oligarchic" growth commences, in which the few largest bodies continue to accrete planetesimals at similar rates.

The picture described above relies upon an important assumption, which is that the mass distribution evolves slow enough for gravitational stirring to maintain energy equipartition. In other words, the relaxation timescale must remain short relative to the growth timescale. For typical conditions near the terrestrial planet forming region of the solar system, this timescale condition is satisfied. Due to the steep dependence of the relaxation time on encounter velocity, this condition can easily be violated at shorter orbital periods.

In figure 1, we show ratio between the relaxation and collision timescale for a population of equal-mass planetesimals as a function of orbital period. Here, the encounter velocity is described by

$$v = \left(5/8 \left\langle e^2 \right\rangle^{1/2} + \left\langle i^2 \right\rangle^{1/2}\right)^{1/2} v_k,$$

(Lissauer & Stewart 1993) where $\left\langle e^2 \right\rangle^{1/2}$ and $\left\langle i^2 \right\rangle^{1/2}$ are the eccentricity and inclination dispersions of the planetesimal disk and v_k is the Keplerian velocity. For simplicity, we assume that $\left\langle e^2 \right\rangle^{1/2} = 2 \left\langle i^2 \right\rangle^{1/2}$ (Ida et al. 1993) and that the eccentricity dispersion is constant with orbital period. The eccentricity dispersion is described in units scaled by the Hill factor $(m_{pl}/3M_\star)^{1/3}$ such that $e_h = 1$ corresponds to the boundary between shear and dispersion dominated encounters. The horizontal dashed line indicates where $t_{relax} = t_{coll}$. The timescale criterion for oligarchic growth is only satisfied in regions where the disk is sufficiently dynamically cold and the orbital period is sufficiently long. In sections 4 and 5 we will explore the behavior and outcome of planetesimal accretion in regions where this criterion is *not* satisfied.

2.2. *Planetesimal Size and Extent of Hill Sphere*

In the formalism described above, the mass and velocity distribution of the bodies are both a function of time. Due to the interdependence of these quantities, it is not clear whether the timescales for gravitational scattering and growth will remain proportional as the oligarchs develop. In the case of many studies of planetesimal accretion in the solar system (cite examples), the $t_{relax} \ll t_{coll}$ condition must remain true, otherwise runaway growth would have continued until all of the planetesimals were consumed. However, it isn't immediately clear what will happen if the system begins in a state where $t_{coll} \ll t_{relax}$.

An insight into the expected behavior in this regime can be gained by defining the dimensionless parameter α, which is the ratio between the physical size of a body and it's Hill radius, r_h:

$$\alpha = \frac{r_{pl}}{r_h} = \frac{1}{a} \left(\frac{9M_\star}{4\pi \rho_{pl}}\right)^{1/3}, \qquad (4)$$

where a is the semimajor axis of the body and ρ_{pl} is its bulk density. Assuming a fixed bulk density as bodies
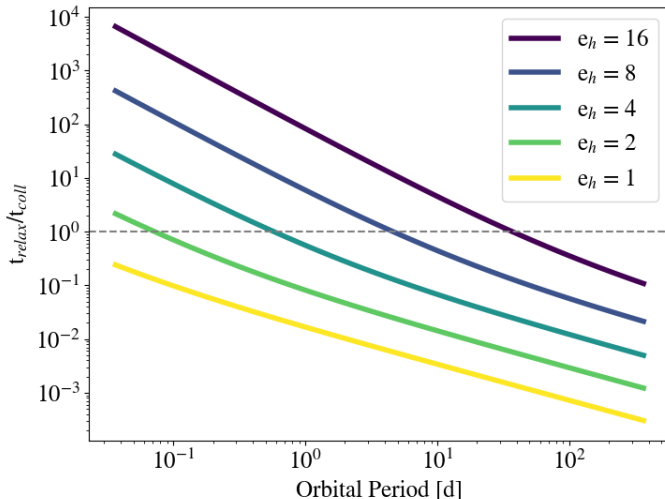
Figure 1. The ratio between the two-body relaxation and collision timescale for a population of equal-mass planetesimals with an internal density of 3 g cm^{-3} and an eccentricity dispersion characterized by e_h, where $e_h = 1$ is the boundary between shear and dispersion dominated encounters. Only in regions where $t_{relax} \ll t_{coll}$ can the velocity distribution respond to changes in the mass of the bodies such that oligarchic growth can operate. This condition is no longer satisfied for a dynamically hot disk at sufficiently short orbital periods.

collide and grow, and that no large-scale migration occurs, the scaling of both r_{pl} and r_h with $m_{pl}^{1/3}$ means that α will be constant with time. For a composition of ice and rock, α is small for any populated region of the solar system ($\alpha \sim 10^{-2}$ for Earth and $\alpha \sim 10^{-4}$ in the Kuiper belt). As one moves close to the star α becomes larger than 1, which implies that the physical extent of a body exceeds its Hill sphere. (also mention that hill sphere size independent of velocity for small eccentricity)

The size of α controls the relative importance of gravitational scattering and collisions in driving the evolution of the planetesimal disk. In the case that α is small, most close encounters will result in a gravitational interaction only, moving the system toward a state of relaxation. If, however, the Hill sphere is largely filled by the body itself, these same encounters will instead drive evolution of the masses. Because α is independent of time, the innermost region of the planetesimal disk, where collisions dominate over scattering events, should remain that way.

We also introduce a second dimensionless quantity, which relates the physical size of the bodies to the velocity state of the system

$$\beta = \frac{r_{pl}}{r_g}. \tag{5}$$

where $r_g = G m_{pl}/v^2$ is the gravitational radius of a body. Encounters between bodies inside of a distance of r_g result in significant deflections of their trajectories. It should be noted that the gravitational focusing enhancement factor v^2/v_{esc}^2 is equal to 1 for $\beta = 1$. In the case where r_g is smaller than the size of a planetesimal, the gravitational focusing enhancement factor will be between 0 and 1.

These scaling considerations motivate the range of parameters in the following numerical experiments as we explore the different regimes.

3. NUMERICAL METHODS

We use the tree-based N-body code CHaNGa[1] to model the gravitational and collisional evolution of planetesimals at short orbital periods (where α is large). CHaNGa is written using the CHARM++ parallel programming language and has been shown to perform well on up to half a million processors (Menon et al. 2015) and can follow the evolution of gravitationally interacting swarms of up to billions of particles. Using a modified Barnes-Hut tree with hexadecapole expansions of the moments to approximate forces, CHaNGa integrates the equations of motion using a kick-drift-kick leapfrog scheme. For all of the simulations presented in this paper, we use a node opening criteria of $\theta_{BH} = 0.7$. Additional information about the code is available in (Jetley et al. 2008; Menon et al. 2015).

Using the neighbor-finding algorithm in CHaNGa, originally designed for SPH calculations, we have recently implemented a solid body collision module in the code. This work is largely based on the solid-body collision implementation in PKDGRAV, which is described in Richardson (1994) and Richardson et al. (2000). To summarize, imminent collisions are detected during the "drift" phase by extrapolating positions of bodies forward in time, using the velocity calculated at the opening "kick". For each body, any neighboring particles which fall within a search ball of radius $2\Delta T v + 2r_{pl}$, where ΔT is the current timestep size for the particle and v is magnitude of its heliocentric velocity, are tested for an imminent collision. In the case that a collision is detected, the particles are merged into a single larger body, which is given the center of mass position and velocity of the two children. Resolving a collision can produce another imminent collision, so collisions are handled one-by-one and another full collision check is run after the previous event is resolved. For a more detailed description of the collision module in

ChaNGa, see (Wallace & Quinn 2019). Particles are advanced in time on individual timesteps chosen as a power of two of a base timestep. The timestep for an individual particle is based on an estimate of the gravitational dynamical time determined by the minimum of $\sqrt{d_{node}^3/(G(M_{node} + m_{pl}))}$ across all nodes in the tree that are accepted by the Barnes-Hut opening criterion. Here d_{node} is the distance from the planetesimal to the center of mass of the tree node and M_{node} is the total mass of the tree node. For nearby particles M_{node} is replaced with the mass of the nearby particle.

4. NARROW ANNULUS SIMULATIONS

We begin by presenting a parameter study of planetesimal accretion, motivated by two questions raised in section 2. 1) Does runaway growth still operate when the condition that $v \ll v_{esc}$ is not satisfied? 2) How does planetesimal accretion proceed when the planetesimals themselves occupy a significant fraction of their Hill spheres?

To answer these questions, we run a series of simulations in which a narrow annulus of planetesimals orbits a star. The values of α and β are varied individually. 4000 planetesimals with individual masses of 5×10^{23} g are placed with semimajor axes randomly drawn between 0.95 and 1.05 AU about a 1 $M_\odot$ star. The argument of perihelion ω, longitude of ascending node Ω, and mean anomaly M for each body is drawn from a uniform distribution $\in [0, 2\pi)$. The inclinations and eccentricities are drawn from a Rayleigh distribution with $\langle i^2 \rangle = 1/2 \langle e^2 \rangle$ (Ida et al. 1993).

In the "fiducial" case, we give the bodies a bulk density of 3 g cm^{-3}, and $\langle e^2 \rangle^{1/2} = 4e_h$, which corresponds to $\alpha = 3.6 \times 10^{-2}$ and $\beta = 3.4 \times 10^{-3}$. These parameters are chosen to match the initial conditions of Kokubo & Ida (1998), which gave rise to oligarchic growth. To vary the value of α, we alter the bulk density of the particles. In the high-α case, the bulk density is reduced by a factor of ~ 7100, which produces $\alpha = 1$. To vary β, the eccentricity dispersion is increased. For the high-β case, $\langle e^2 \rangle^{1/2}$ is increased to $1500e_h$, which corresponds to $\beta = 15,000$.

In all cases, the simulations are evolved with a base timestep of 1.7 days, which corresponds to 3% of an orbital dynamical time $\sqrt{a^3/GM_*}$. Due to the vastly differing growth timescales in each case, a simulation is stopped when the growth of the most massive body flattens out. In figure 2, we show the a-e distribution of bodies in the initial (blue) and final (orange) snapshots from each of the 4 simulations. The size of the points indicates the relative masses of the bodies. Only in the case of small α does a residual population of dynamically hot planetesimals develop. The lack of high eccentricity planetesimals in the large α case suggests that most encounters result in accretion instead of scattering. In the case of large β, the protoplanets and remaining planetesimals end up in a dynamically cool state, compared with the initial conditions. This is due to kinetic energy being lost as particles inelastically collide. One final point to note is the difference between eccentricities of the protoplanets in the large α, large β and the small α, large β case. The dynamically cooler result of the latter case is likely due to the dominant role that inelastic collisions play here.

In figure 3, we show the mass distribution of bodies from the final snapshot in each of the four cases. In addition to leaving fewer residual planetesimals, the large α simulations produce significantly larger embryos. Despite the vastly different encounter velocities of each population of bodies, the initial size of β (so long as bodies remain in the dispersion-dominated regime) appears to have no significant effect on the final distribution of masses.

To investigate whether any of these planetesimal rings underwent runaway growth, we examine the time evolution of the maximum and mean masses in each simulation. The ratio $m_{max}/\langle m \rangle$ is plotted in figure 4. On this plot, a positive slope indicates that the maximum and mean masses are diverging (i.e. the growth rate is accelerating with mass), which is evident for every case we have tested. Even with a large β, which means that the effective collision cross section is very near the geometric value, runaway growth still appears to operate. The ubiquity of the early positive trends in this figure indicates that, as bodies collide and grow the relative difference in gravitational focusing factors between bodies is what drives the system towards runaway growth. Although larger encounter velocities lengthen the growth timescales, this mode of growth appears to be inevitable, so long as gravity is the dominant force in the system. For the large α cases, the curves in this figure eventually turn over and begin to decline. Upon inspecting the simulation snapshots, we find that this trend is driven by an increase in the average mass as the planetesimal population becomes depleted. One should expect that the same thing will eventually occur for small α, although many more timesteps are required to begin to run out of planetesimals.

Additionally, these results suggest that the value of α, which is a function of only the initial conditions (the physical and Hill radius both scale with $M^{1/3}$, so α stays constant as bodies grow), controls the qualitative outcome of accretion. Across most of a planet-forming disk, α is small, and frequent gravitational en-

Table 1. Summary of Full Disk Simulations Run

Name	m_{pl}^a	N_{pl}^b	A^c	α^d
fdHi	5×10^{22}	903,687	100	1.5
fdHiShallow	5×10^{22}	903,687	100	0.5
fdHiSteep	5×10^{22}	903,687	100	2.5
fdLo	5×10^{22}	45,185	1	1.5

NOTE
[a] Planetesimal mass [g]
[b] Number of planetesimals
[c] Solid surface density normalization (relative to MMSN)
[d] Solid surface density power law index

counters between the growing bodies will facilitate oligarchic growth. In the dispersion-dominated regime, close encounters drive the stirring between planetesimals and embryos (Weidenschilling 1989; Ida 1990). When α is large, the Hill sphere of a body is no longer mostly empty space, and close encounters that would otherwise result in stirring instead result in accretion. In this regime, we observe that runaway growth still commences, but nearly all of the planetesimals are swept up by the forming protoplanets, rather than being scattered onto higher eccentricity orbits, where they would otherwise remain as a remnant of the early stages of planet formation (Kokubo & Ida 1998, 2000).

5. FULL DISK SIMULATION

5.1. *Initial Conditions*

Motivated by the dependence of accretion modes on α, we next investigate whether this highly efficient, non-oligarchic growth should be expected to operate near the innermost regions of a typical planet-forming disk. Given that N-body simulations of short-period terrestrial planet formation typically begin with a chain of neatly-spaced, isolation mass (see Kokubo & Ida (2000) eq. 20) protoplanets, it is pertinent to determine whether the high α growth mode we revealed in the previous section invalidates this choice of initial conditions.

Given the dearth of short-period terrestrial planets observed around M stars (e.g. TRAPPIST-1), we chose to model the evolution of a series of wide planetesimal disks, which span from 1 to 100 days in orbital period, orbiting a late-type M star of mass 0.08 $M_\odot$. For a population of planetesimals with a bulk density of 3 g cm^{-3}, this orbital period range corresponds to $\alpha \in (0.7, 0.05)$. By simultaneously modeling a broad range of orbital periods, we can determine the critical value of α that divides these two modes of accretion, and also explore how the oligarchic/non-oligarchic accretion boundary affects the resulting distribution of protoplanets.

Four wide-disk simulations are run in total (see table 1). In each case, the solid surface density follows a power law profile

$$\Sigma(r) = \left(\frac{M_*}{M_\odot}\right) A \Sigma_{\mathrm{MMSN}} \left(\frac{r}{1\mathrm{AU}}\right)^{-\delta}, \quad (6)$$

where M_* is the mass of the central star, $\Sigma_{MMSN} = 10$ g cm^{-2} is surface density of the minimum-mass solar nebula (Hayashi 1981) at 1 AU, and A is an enhancement factor. In the first case (fdHi), we model a disk that follows a MMSN power law slope, with the overall normalization enhanced by a factor of 100. This choice of normalization for the solid surface density profile appears necessary in order to reproduce many observed short period terrestrial worlds in-situ (Hansen & Murray 2012). Additionally, we vary the power law index (fdHiShallow, fdHiSteep) and overall normalization (fdLo) of $\Sigma(r)$.

In all cases, the eccentricities and inclinations of the bodies are randomly drawn from a Rayleigh distribution, with $\langle e^2 \rangle^{1/2} = 2 \langle i^2 \rangle^{1/2} = e_{eq}$. The value of e_{eq} is chosen such that the timescales for viscous stirring and aerodynamic gas drag on the planetesimals are in equilibrium. The viscous stirring timescale is given by Ida & Makino (1993) as

$$\tau_{vs} = \frac{\langle e^2 \rangle}{d \langle e^2 \rangle / dt} \approx \frac{1}{40} \left(\frac{\Omega^2 a^3}{2Gm_{pl}}\right)^2 \frac{4m_{pl} \langle e^2 \rangle^2}{\Sigma a^2 \Omega}, \quad (7)$$

where Ω, a and e are the orbital frequencies, semimajor axes and eccentricities of the individual planetesimals. In the Stokes regime, the gas drag timescale is given by Adachi et al. (1976) as

$$t_s = \frac{2m_{pl}}{C_D \pi r_{pl}^2 \rho_g v_g}, \quad (8)$$

where C_D is a drag coefficient of order unity, ρ_g is the local gas volume density and v_g is the headwind velocity of the gas experienced by the planetesimal. The local gas volume density is given by

$$\rho_g = \frac{\Sigma_g}{\sqrt{2\pi} h_g \exp\left[-z^2 / \left(2h_g^2\right)\right]}, \quad (9)$$

where Σ_g is the gas surface density (taken to be 240 times the solid surface density), $h_g = c_s/\Omega$ is the local gas scale height and z is the height above the disk midplane. The sound speed profile is given by $c_s = \sqrt{k_B T(r) / (\mu m_H)}$, where k_B is Boltzmann's constant, $T(r) = T_0 r^{-Q}$, $\mu = 2.34$ and m_h is the mass of a hydrogen atom. For a protoplanetary disk around a typical M star, $T_0 = 148$ K and $Q = 0.58$ (Andrews & Williams 2005).

Finally, the headwind velocity of the gas, due to the fact that the gas disk is pressure supported, is given by

$$v_g = v_k \left[1 - \sqrt{Qc_s^2/v_k^2} \right], \quad (10)$$

where v_k is the local Keplerian velocity. As in section 4, the argument of perihelion ω, longitude of ascending node Ω, and mean anomaly M for the planetesimals are drawn from a uniform distribution $\in [0, 2\pi)$.

5.2. Gas Drag Force

In addition to the mutual gravitational forces, a Stokes drag force from to the gas disk is applied to each particle, following the prescription described in section 2.2.1 of Morishima et al. (2010).

5.3. Timestepping Criterion

In the case of the fdHi simulation, there are nearly 1 million particles, whose orbital periods vary by two orders of magnitude. Because the interaction timescales near the inner edge of the disk are exceedingly short, a fixed timestep size would required a prohibitively large number of steps to follow planetesimal growth throughout the entire disk. For this reason, we use a multi-tiered timestepping scheme, in which particles are placed onto the nearest power of two timestep based on their most recently calculated gravitational acceleration. [2]

This more efficient scheme introduces two issues, however. Firstly, momentum is not completely conserved when bodies switch timesteps. The error introduced becomes particularly severe for a particle on an eccentric Keplerian orbit, whose perihelion and aphelion distances straddle a timestep boundary. For a large collection of particles, this problem manifests itself as the development of a V-shaped gap in the semimajor axis-eccentricity plane, which is centered on the boundary itself. To correct this problem, we introduce a slightly modified timestepping criterion, which is based on the expected gravitational acceleration of the particle at pericenter. Only in the case of a close encounter with another planetesimal (in which the acceleration is no longer dominated by the star) is the timestep allowed to reduce based on the original criterion.

A second issue is introduced when two particles on different timesteps undergo a collision. As in the previous case, momentum is not completely conserved because the most recent 'kick' steps did not happen simultaneously for these bodies. Early in the simulation, we find that runaway growth tends to initiate at the timestep

Table 2. Final Properties of Full Disk Simulations

Name	M_{PP}^a	T_{int}^b	T_{int1}^c
fdHi	1.00	456	16,377
fdHiShallow	1.19	456	16,377
fdHiSteep	1.08	456	16,377
fdLo	1.77 $\times 10^{-3}$	3,713	133,651

NOTE
[a] Maximum protoplanet mass $[M_{earth}]$
[b] Integration time [yr]
[c] Rescaled integration time [yr]

boundaries. This issue carries itself forward through the embryo formation phase, and protoplanets tend to form at the boundaries. To correct this issue, we ignore collisions between bodies on different timesteps early in the simulation. We find that preventing multi-timestep collisions until after the maximum mass grows by a factor of 10 prevents any artifacts from developing at the timestep boundaries, while also minimizing the number of 'skipped' collisions[3].

5.4. Results

The timescales for embryo formation depend on the chosen surface density profile, along with the local orbital timescale. Protoplanets form first at the inner edge of the disk, where the dynamical timescales are short. Growth proceeds in an inside-out fashion, with the outermost regions of the disk completing the protoplanet assembly phase last. This radial timescale dependence is not typically accounted for in planet formation simulations[4], and appears to be an important component to forming realistic solar system analogs (Clement et al. 2020). As with the narrow annulus simulations, we stop the integration once the masses of protoplanets in the outermost region of the disk reach a steady value. In table 2, we summarize the outcomes of the four "full disk" cases.

We show the final state of the "fdHi" simulation in figure 5. In the top panel, the initial (contours) and final (points) state of the simulation is shown in the orbital period-eccentricity plane. The size of the points indicates the relative mass of the bodies. In the bottom panel, the mass of the largest bodies is shown as a function of orbital period. The solid curves indicate the

---

[2] This scheme is used on almost all works using ChaNGa, and is common among large-scale simulation codes.

[3] In the case of fdHi, only about 20 collisions out of an eventual 900,000 are ignored.

[4] Instead, the innermost protoplanets patiently 'wait' for this phase of evolution to complete everywhere in the disk

isolation mass,

$$M_{iso} = \left[\frac{\left(2\pi a^2 \Sigma \tilde{b}\right)^3}{3M_*} \right]^{1/2}, \qquad (11)$$

where $\tilde{b}$ is the size of the feeding zone in units of Hill radii. For a body on a circular orbit $\tilde{b} = 2\sqrt{3}$, while a protoplanet formed by oligarchic growth typically has $\tilde{b} = 10$ (Kokubo & Ida 1998). The isolation mass is plotted in blue and orange for these two values of $\tilde{b}$, respectively.

A qualitative shift in the protoplanet and planetesimal distribution is visible at ~ 60 days. Interior to this location, there are very few remaining planetesimals and the embryos formed are noticeably more massive. Protoplanets in this region appear to closely follow the isolation mass curve for $\tilde{b} = 10$. Exterior to the boundary, the residual planetesimal population is much more numerous, and protoplanets more closely follow the $\tilde{b} = 2\sqrt{3}$ curve. This suggests that the transition between the low α and high α accretion modes seen in section 4 happens near this location.

In section 4, we postulated that the increased importance of inelastic damping in the inner, non-oligarchic growth region of the disk should lower the overall eccentricity of the protoplanets there. This behavior is not immediately apparent in the top panel of figure 5. There are, however, a couple of factors in the wide disk simulations that could make this extra dynamical cooling mechanism difficult to see. Firstly, the initial eccentricity distributions of the inner and outer disk are different because of the dependence of the viscous stirring and gas drag timescales on orbital period. Additionally, the protoplanet formation timescales for the inner and outer disk are vastly different, rendering a comparison between these regions at the same moment in time inappropriate.

To ensure that the boundary seen near 60 days in orbital period is not simply a transient product of the inside-out growth throughout the disk, we examine the time evolution of σ/Σ at multiple locations. In figure 6, the value of σ/Σ is plotted as a function of time in 10 orbital period bins, each with a width of 10 days. Bins interior to 60 days are indicated with a dashed line, while those exterior are indicated with a solid line. The planetesimal surface density fraction has decelerated and is approaching an asymptotic value in all cases. In the inner disk, this is driven by the near-total depletion of the planetesimal reservoir. In the outer disk, dynamical friction between the embryos and planetesimals throttles subsequent accretion.

Next, we compare the effect of varying the initial solid surface density profile on the resulting planetesi-mal and embryo distribution. The final orbital period-eccentricity state of the particles is shown in figure 7, with colors and point styles indicating the different initial surface density profiles, and with point sizes indicating the relative masses of the bodies. There is a clear trend between solid surface density at a given orbital period and the eccentricities of the remaining planetesimals. This trend is largely set by the initial conditions, as the gravitational stirring is more vigorous when bodies are packed together closely and higher eccentricities are required to produce an equilibrating aerodynamic drag force (see equations 7 and 8). Despite having significantly different masses, the planetary embryos formed in each case have remarkably similar eccentricities. This is likely due to the fact that inelastic collisions play a more significant role where the solid surface density is highest, which offsets the fact that the initial bodies started off in a dynamically hotter state.

In figure 8, we compare the masses of the resulting protoplanets and planetesimals in all four simulations to each other. Here, the masses are scaled by the isolation mass at the given orbital distance (see equation 11). In all four cases, the masses follow a similar trend: interior to about 60 days in orbital period, protoplanets grow to a factor of a few larger than M_{iso}. Exterior to this point, the protoplanet masses roughly stay near the isolation mass. Despite the drastically different solid surface density profiles used, the masses of the largest bodies in all four cases follow a similar trend with orbital period. This indicates that the highly efficient accretion mode seen at shorter orbital periods is dependent on the sizes of the individual bodies themselves, rather than how they are distributed. The transition visible near 60 days in all cases also supports our conclusion that planetesimal accretion is largely complete everywhere in the disk.

5.5. *Assembly History of Embryos*

Further insight into the difference between the short vs long period accretion modes can be gained by examining the merger history of the planetary embryos. Because all collisions are directly resolved by the N-body code, a direct lineage can be traced between each embryo and a set of initial planetesimals.

We begin by investigating the "smoothness" of the accretion events that give rise to each embryo. Drawing from a common technique used for cosmological simulations (citation?), we divide growth events for a given body into "major" and "minor" mergers. Minor events are defined as any collision involving an initial planetesimal, while major events consist of any two larger bodies. In figure 9, we show the total mass fraction gained by
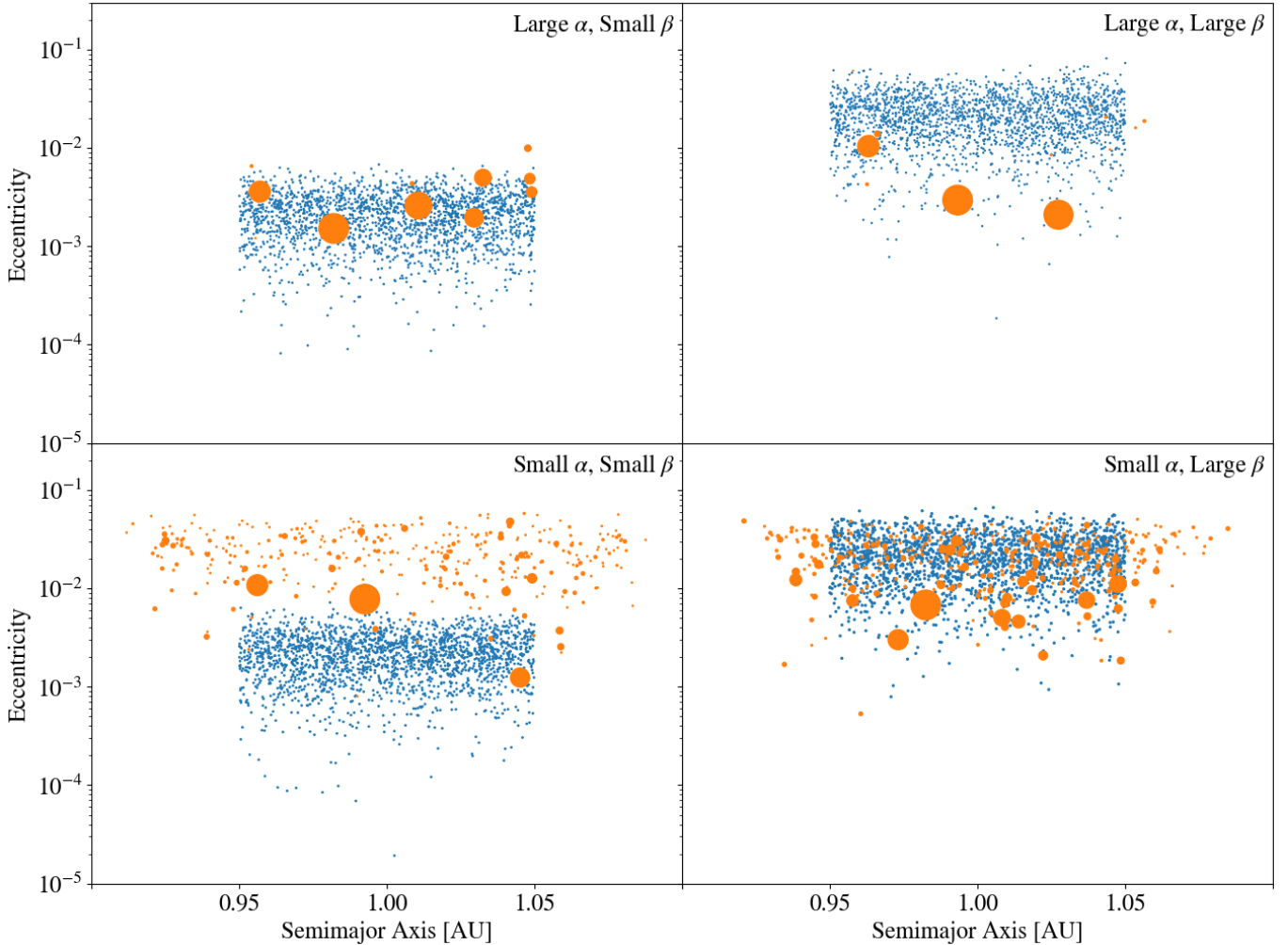
Figure 2. The initial (blue) and final (orange) states of the simulations described in section 4. Relative masses of the bodies are indicated by point size. In the case of large α, almost no residual planetesimal population remains. Regardless of the initial choice of β, the protoplanets that form attain similar eccentricities.

minor events as a function of mass for the 100 largest bodies at the end of fdHi. Blue dots represent bodies interior to the 60 day orbital period boundary, while red crosses indicate bodies exterior. For the outer bodies in the oligarchic growth region, we see a very weak trend between minor accretion mass fraction and total mass. Regardless of how much an embryo has grown, the initial mass planetesimals contribute about the same relative amount to its total mass. At shorter orbital periods, however, there is a somewhat stronger trend. The largest bodies in this region gain about an order of magnitude more of their mass fraction from major mergers, compared to the smallest bodies.

The difference in slope of the short vs. long period bodies in figure 9 indicates a difference in how the planetesimal-embryo populations interact in each region. In the long period oligarchic growth region, embryos continue to accrete planetesimals as they grow and the minor mass fraction stays mostly flat. At short period, collisions mostly occur between equal mass bodies as the embryos grow and the contribution from planetesimals becomes less significant over time. This suggests that embryo-embryo collisions are common at short period. As discussed in section 2.2, the importance of gravitational scattering is greatly reduced here. Without frequent gravitational interactions between the embryos and planetesimals, orbital repulsion (Kokubo & Ida 1998) and isolation of the embryos does not occur. As we showed in figure 8, the embryos formed in this region exceed the isolation mass.

Further evidence for the lack of gravitational scattering events in the inner region can be seen in figure 10. Here, we have chosen the 20 most massive bodies from the fdHi simulation and arranged them in order of
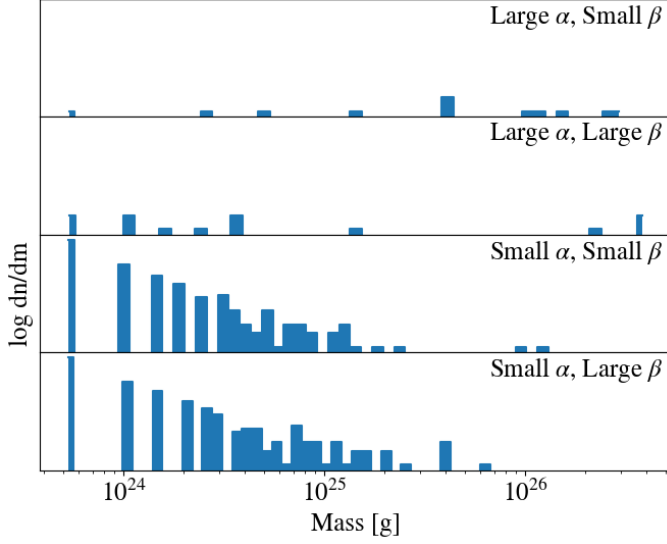
Figure 3. The final state of the mass distribution for the simulations described in section 4. For small α, a few embryos form alongside a power law tail of planetesimals. For larger values of α, the mass distribution takes on a more unimodal (TRQ: uniform?) form. As in the previous figure, the initial choice of β does not appear to have any meaningful impact on the end result.
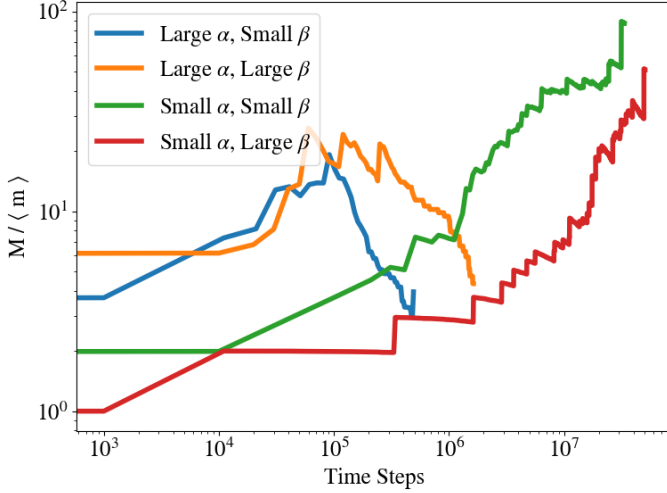

Figure 4. The evolution of the ratio between the maximum and mean mass for the four simulations presented in section 4. The runaway growth phase can be identified by a positive slope in this ratio. For all values of α, an increase in β has the effect of delaying the growth of the embryos.

present orbital period. The vertical black line indicates the orbital period of each embryo. The associated histogram for each body denotes where the planetesimals used to construct that embryo originated in the disk. The peaks of the histograms have all been normalized
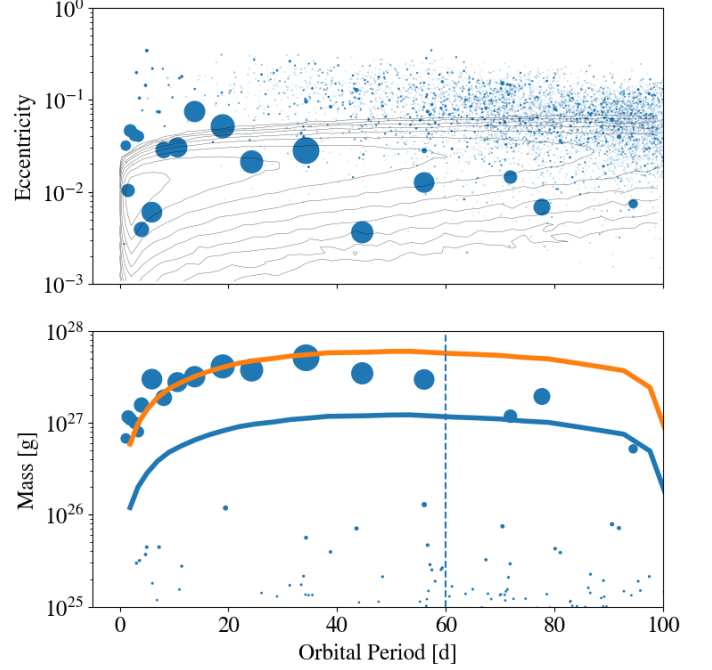
Figure 5. The final state of the fdHi simulation. In the top panel, the contours denote the initial period-eccentricity distribution of the planetesimals. Point sizes indicate the relative masses of bodies. In the bottom panel, the solid line indicates the isolation mass for $\tilde{b} = 2\sqrt{3}$. The vertical dashed line marks the approximate location of the accretion mode boundary. For $P_{orb} < 60$ days, the high α accretion mode produces embryos that exceed the isolation mass.
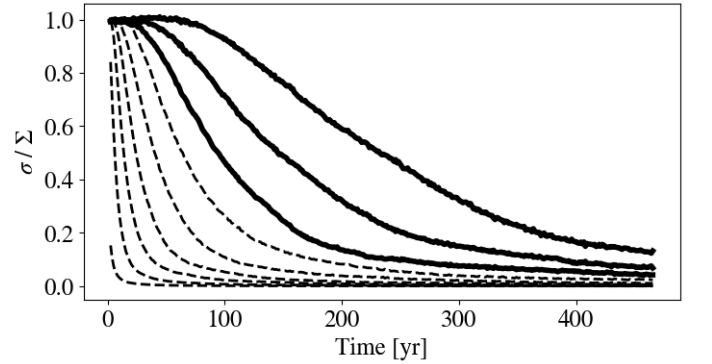
Figure 6. The time evolution of the planetesimal surface density (in units of the total solid surface density) in the fdHi simulation. Each curve represents a radial slice of the disk. The innermost region evolves the quickest, and is therefore represented by the lowest curve. The dashed lines indicate radial zones interior to the 60 day orbital period boundary.
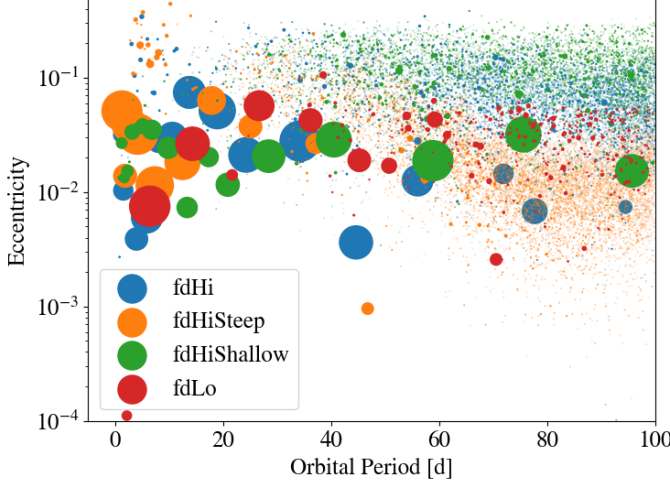
Figure 7. The final state of all simulations listed in table 2. Point sizes indicate mass relative to the largest body in the fdHi simulation.
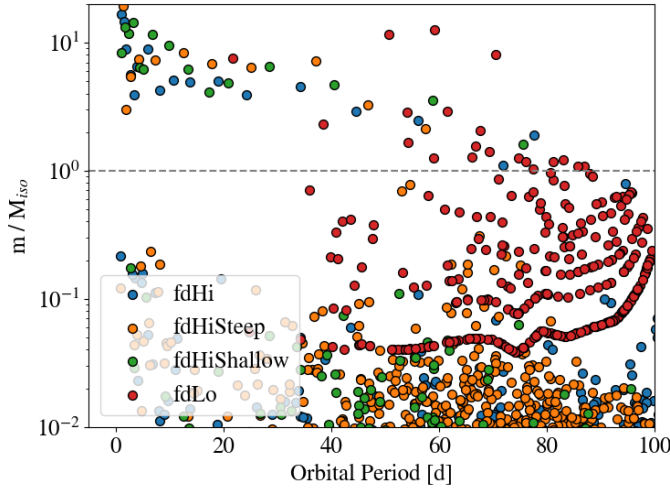

Figure 8. Masses of the remaining bodies from the simulations listed in table 2, in units of the isolation mass for $\tilde{b} = 2\sqrt{3}$. Despite the vastly different initial solid surface density profiles, the orbital period inside of which the embryo masses exceed the isolation mass is very consistent.

to the same value, so that the distributions only show the relative widths and locations of the feeding zones. Beyond the 60 day boundary, the ordering of the feeding zones and the embryo locations become much less consistent. This suggests that scattering events between embryos are much more common beyond this accretion mode boundary. In the inner region of the disk, close encounters between embryos often result in a merger, which allows them to grow beyond the isolation mass with only a minor alteration to their orbital period. With few close encounters resulting in a scattering event,
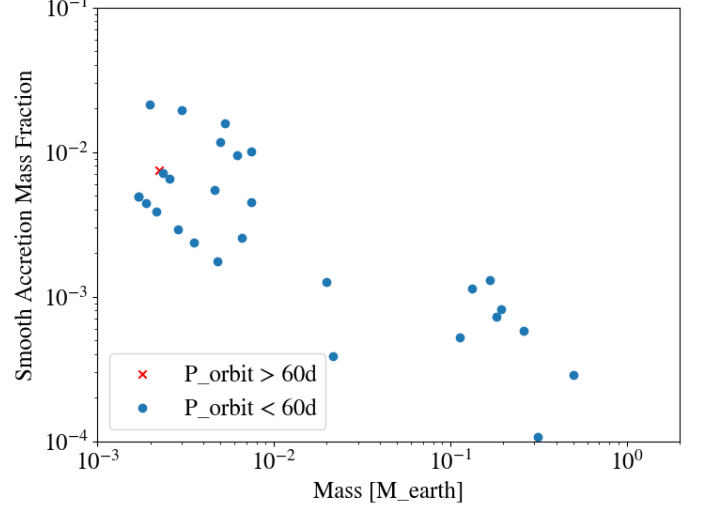
Figure 9. For the 100 most massive bodies at the end of the fdHi simulation, the fraction of their total mass attained through mergers with initial mass planetesimals (smooth accretion) as a function of total mass. Bodies that reside beyond the 60 day accretion boundary are shown with red crosses, while bodies interior to the boundary are shown with blue dots. For the short period bodies, there is a decreasing correlation between smooth accretion fraction and mass, which suggests that most growth occurs between equal mass bodies. For the longer period bodies in the oligarchic growth region, this trend is flat, indicating that accretion of planetesimals is important during all phases of evolution.

embryos are unable to move away from their birth location.

6. SIMPLIFYING ASSUMPTIONS

6.1. *Collision Cross Section*

In all cases shown so far, the boundary between the standard oligarchic growth and the highly-efficient short period accretion region lies around 60 days in orbital period. The mode of accretion is set entirely by the local value of α, which scales with both distance from the star and the bulk density of the planetesimals (see equation 4). The artificial inflation of the collision cross section of the particles in our simulations, which is meant to reduce the computational expense, has the side effect of reducing the bulk densities. Because $\alpha \sim \rho_{pl}^{-1/3}$, increasing the particle sizes by a factor of $f = 6$ reduces the orbital period at which α has a given value by a factor of approximately 15. Therefore, one would expect the accretion boundary to lie near 5 days in orbital period for 3 g cm^{-3} bodies.

Although a simulation with $f = 1$ is not computationally tractable, we can test whether the accretion boundary moves in the way we expect by modestly changing the value of f. In figure 11, we compare the fdHi simu-
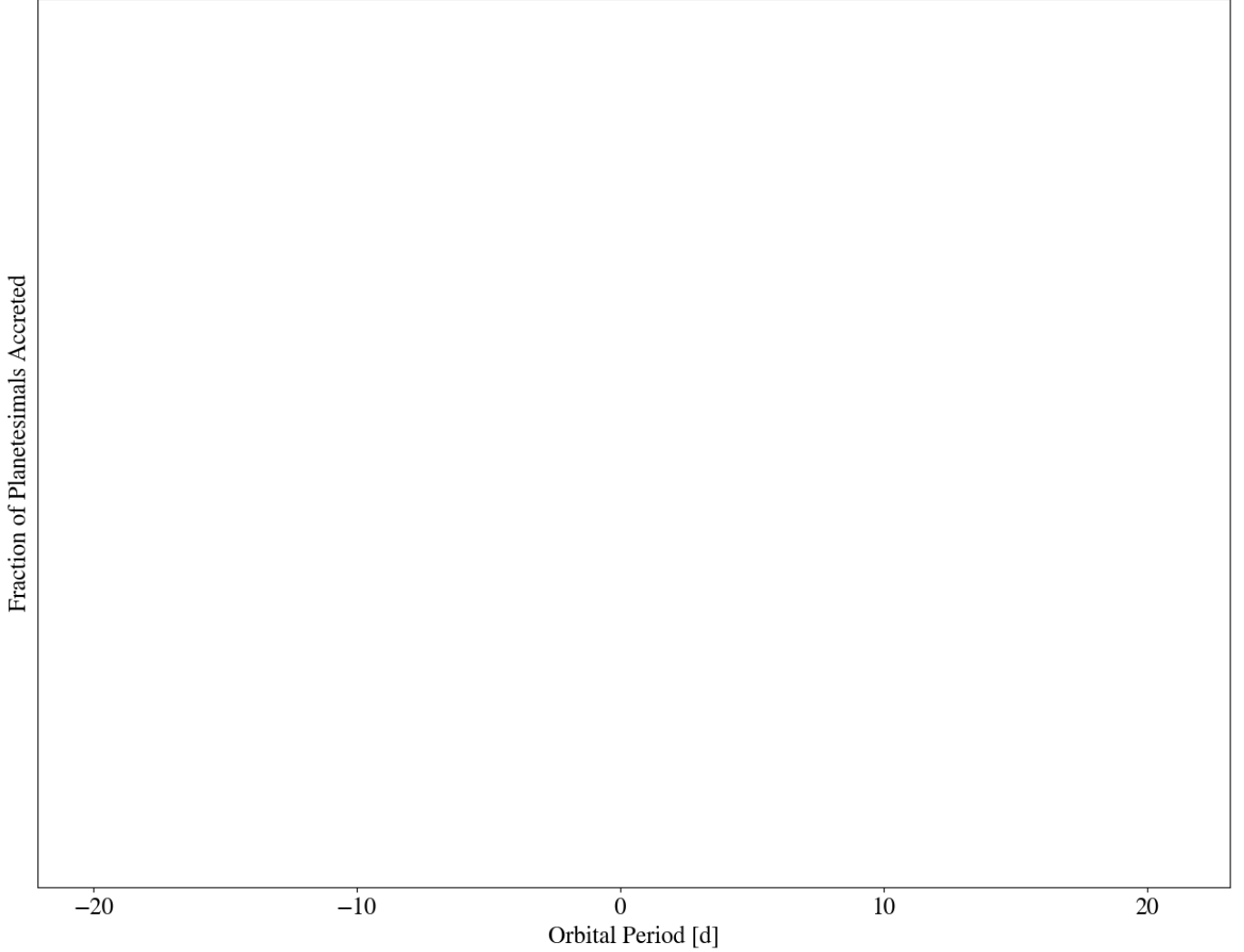
Figure 10. For the 20 most massive bodies at the end of the fdHi simulation, the relative shape of the accretion zones for each body are shown. The black hash marks indicate the present position of the body. The accretion distributions indicate the initial locations of the planetesimals that were used to assemble a body, rather than the locations at which collisions with the massive body occurred.

lation to a nearly identical run using $f = 4$. In the top panel, the embryo masses in units of the isolation mass are shown as a function of orbital period. In the bottom panel, the value of α as a function of orbital period is shown for 3 g cm^{-3} bodies with an artificial radius enhancement of $f = 1$, 4 and 6. The horizontal dashed line indicates the value of alpha below which the accretion mode switches to oligarchic growth. Comparing the top and bottom panels, the intersection of the embryo masses and local isolation mass matches well with the orbital period at which $\alpha \sim 0.1$. Also shown by the shaded region are α values for realistic sized bodies with ρ_{pl} between 1 and 10 g cm^{-3}. In all cases, the accretion boundary still lies within the part of the disk in which solids would be expected to accumulate (citation?).

6.2. Collision Model

In the simulations presented in this work, all collisions result in a complete merging of a pair of bodies with no loss of mass or momentum. Although simple to model, this assumption of perfect accretion may result in overly efficient growth, particularly at the innermost region of the disk where encounter velocities are the largest. To handle this issue properly, semianalytic collision resolution models have been developed and implemented in N-body codes (see Leinhardt & Stewart (2012)). However, resolving collisional debris fragments using a direct approach as we have done with CHANGA would result in an intractably large number of particles.

To test whether a more restrictive collision model should modify our results, we present a smaller scale
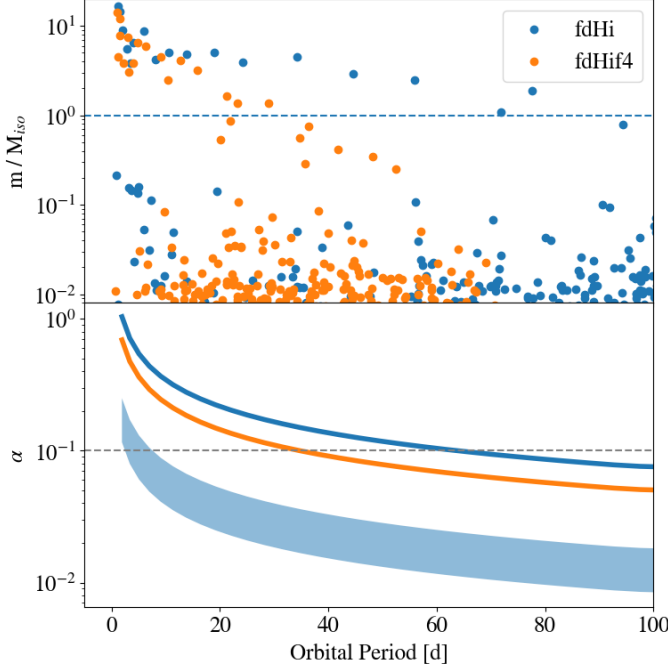
Figure 11. In the top panel, we show the final masses of the bodies from the fdHi and fdHif4 simulations in units of the isolation mass for $\tilde{b} = 2\sqrt{3}$. The bottom panel shows the variation of α with orbital period for the bodies used in each case (solid curves). The orbital period at which $\alpha \simeq 0.1$ matches well with the intersection of the embryo mass distribution and isolation mass. The shaded region in the bottom panel show the values of alpha for realistic-sized ($f = 1$) planetesimals with bulk densities between 10 and 1 g cm^{-3}.

test using a slightly more sophisticated collision model. In this case, a collision can result in one of two outcomes: if the impact velocity is smaller than the mutual escape velocity of the colliding particles, defined as

$$v_{mut,esc} = \sqrt{\frac{G(m_1 + m_2)}{r_1 + r_2}}, \qquad (12)$$

where m_1, m_2 and r_1, r_2 are the masses and radii of colliding particles 1 and 2, then the bodies perfectly merge. For impact velocities larger than $v_{mut,esc}$, no mass is transferred, and the bodies undergo a completely elastic bounce. Because there is no possibility of partial accretion, this model likely restricts growth more than the model used by Leinhardt & Stewart (2012). However, we will show below that the bounce-merge model does not meaningfully affect the outcome of the planetesimal accretion phase, and so a partial accretion model should do the same.

For the configuration of initial conditions we have chosen, the typical encounter velocity (defined by $v_{enc} = \langle e^2 \rangle^{1/2} v_k$, where v_k is the local Keplerian velocity) is
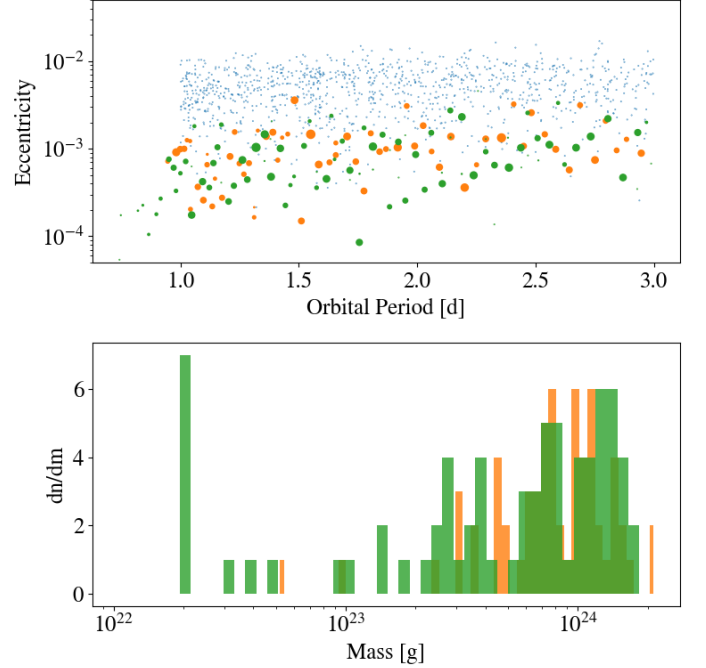

Figure 12. A comparison between the innermost regions of the fdLo (orange) simulation, and a second version using a bounce-merge collision model (green). In the top panel, the period-eccentricity state of the particles is shown, with marker sizes indicating relative mass. The blue points represent the initial state of the simulations. The bottom panel compares the final masses of the bodies.

about 25 percent larger than $v_{mut,esc}$. Because the encounter velocities follow a Gaussian distribution, there should be some small subset of collisions that still meet the merger criteria. In addition, $v_{mut,esc}$ becomes larger as the bodies grow and the merger criteria should become easier to meet as the system evolves.

In figure 12, we show the results of two versions of the fdLo simulation, one with mergers only (shown in orange) and one with the bounce-merge model (shown in green). The blue points in the top panel show the initial conditions used for both cases. Because the bounce-merge model greatly increases the number of timesteps required, we choose to model only the innermost part of the disk to reduce the computational cost. Although the bounce-merge simulation takes much longer to reach the same phase of evolution, the resulting orbits and masses of the embryos are indistinguishable from the merger-only case.

To investigate the differences between the two collision models early in the simulations, we show the time evolution of the ratio between the maximum and mean mass in figure 13. In both cases, this ratio grows at early times, which indicates that runaway growth still
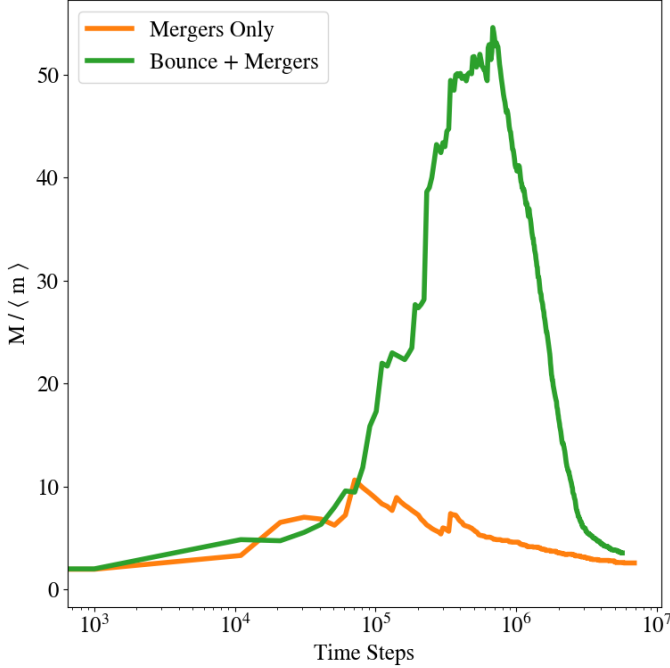
Figure 13. The evolution of the ratio between the maximum and mean mass of the simulations shown in figure 12. In both cases, the system first evolves through a phase of runaway growth, before the massive bodies consume the smaller bodies, driving down the mean mass. With the bounce-merge model, the mass ratio decreases later because not all collisions result in growth.

ual planetesimals. This corresponds to the "oligarchic growth" case revealed by (Kokubo & Ida 1998). In the second mode, the gravitational feedback does not operate, embryos quickly sweep up all planetesimals, and grow about twice as large as is predicted by oligarchic growth. The distinction between these modes is determined by ratio between the physical size of the bodies and their Hill radius.

We have demonstrated the outcome of both accretion modes through a sparsely sampled parameter study. The initial planetesimal distribution can be described in terms of two dimensionless constants, α and β, which describe the ratio between the physical radius of the planetesimals and the Hill (r_h) and gravitational (r_g) radii, respectively. For a fixed planetesimal mass and radius, α scales with the orbital period and β scales with the level of dynamical excitation of the disk. We showed that $\alpha \ll 1$ leads to oligarchic growth, while a non-negligible α produces this new non-oligarchic growth mode. We find that the resulting mass distribution, along with the final eccentricities of the embryos and residual planetesimals, ends up the same, regardless of the initial value of β.

So long as the density of the bodies does not significantly change as their mass distribution evolves, this ratio, and therefore the boundary between these accretion modes is set entirely by the distance from the star. Because both the physical and Hill radii of the bodies grows as $M^{1/3}$, the boundary between growth remains at a fixed location in the disk during the planetesimal accretion process.

We have verified this fact by testing the outcome of the planetesimal accretion process for a variety of solid surface density profiles. Although altering the surface density does affect the resulting masses of the embryos, the location of the boundary separating the growth modes is remarkably similar among all of our simulations. We have verified this by comparing the resulting embryo masses to the isolation mass, in addition to highlighting qualitative differences in the accretion history of embryos on both sides of the boundary.

Lastly, we quantified the way in which our use of perfect accretion and an inflated collision cross section, both meant to make the simulations more computationally tractable, affect the non-oligarchic growth mode and the location of the accretion boundary. We showed that although the use of perfect accretion speeds up the growth of the embryos, it does not affect the masses or orbital properties of the resulting bodies. Because the inflated collision cross sections artificially reduce the density of the planetesimals, this shortcut does shift the accretion boundary outward. However, it moves in a predictable

operates, regardless of the collision model used. In the bounce-merge case, the mass ratio peaks at a higher value, while also undergoing a longer runaway growth phase. This suggests that the mass distribution becomes much less unimodal during this growth process, but as figure 12 shows, this does not affect the resulting embryos or allow for a residual planetesimal population.

Radial mixing appears to be enhanced by a partial collision model, along with smaller collision cross section inflation (Childs & Steffen 2022).

6.3. *Type I Migration*

What is the migration timescale for the embryos to move to the inner edge of the disk? Maybe this section isn't terribly important and should be excluded? TRQ: I agree

7. SUMMARY AND DISCUSSION

In this work, we have demonstrated that planetary embryo formation operates in two distinct modes in a planet-forming disk. In the first mode, gravitational feedback from the growing embryos heats the remaining planetesimals and results in a dynamically cold population of embryos with a significant amount of resid-

fashion and we verified this by running an extra simulation with a modestly smaller collision cross section. In a real planet-forming disk, one would expect this boundary to lie somewhere between 2 and 10 days, depending on the composition of the planetesimals.

To date, there have been no other studies of planetesimal accretion with such a large value of α. However, a value of $\alpha = 1$ corresponds to the Roche limit of a three-body system, and so one might wonder this high-α accretion mode might be relevant for a circumplanetary system. There is a small collection of previous works which use N-body methods to examine in-situ satellitesimal accretion (Ida et al. 1997; Richardson et al. 2000; Ida et al. 2020). Ida et al. (1997) was able to form 1-2 large moons just exterior to the Roche limit, depending on the extent of the disk with very little satellitesimal material left over. The widest disk they modeled extended out to $\alpha = 0.5$. Qualitatively, this result is very similar to the short period planetesimal accretion mode observed in our simulations. Ida et al. (2020) modeled a much wider satellitesimal disk, which extends out to about $\alpha \approx 0.05$. Inside to the $\alpha = 0.1$ accretion boundary (which lies near $15 R_U$ in figure 1 of Ida et al. (2020)), bodies grow beyond the isolation mass, while the opposite is true on the other side of the boundary. In addition, a residual population of satellitesimals is still present beyond the boundary, which suggests that oligarchic growth is indeed operating on the far side.

Presently, the implications that this non-oligarchic accretion mode has for the formation of short-period terrestrial planets, and whether the accretion boundary would leave any lasting imprint on the final orbital architecture, is unclear. One point that our results do highlight is that the initial conditions used for most late stage planet formation simulations are overly simplistic. Clement et al. (2020) recently simulated planetesimal accretion in a disk extending from the orbit of Mercury to the asteroid belt and found that the disk never reaches a state in which equally-spaced, isolation mass embryos are present everywhere simultaneously. Instead, different annuli reach a 'giant impact' phase at different times, preventing the onset of a global instability throughout the entire disk, as is common in classic terrestrial planet formation models (Chambers & Wetherill 2001; Raymond et al. 2009).

To connect these accretion modes to the final orbital architecture, and to ultimately determine what implications an in situ formation model has for the growth of STIPs, we will continue to evolve the final simulation snaphots presented here with a hybrid symplectic integrator. The final distribution of planets formed, along with composition predictions generated by applying cosmochemical models to our initial planetesimal distributions and propagating compositions through the merger trees, will be examined in a follow-up paper.

REFERENCES

Adachi, I., Hayashi, C., & Nakazawa, K. 1976, Progress of Theoretical Physics, 56, 1756, doi: 10.1143/PTP.56.1756

Andrews, S. M., & Williams, J. P. 2005, ApJ, 631, 1134, doi: 10.1086/432712

Bai, X.-N., & Stone, J. M. 2010, ApJ, 722, 1437, doi: 10.1088/0004-637X/722/2/1437

Barnes, R., Quinn, T. R., Lissauer, J. J., & Richardson, D. C. 2009, Icarus, 203, 626, doi: 10.1016/j.icarus.2009.03.042

Beitz, E., Güttler, C., Blum, J., et al. 2011, ApJ, 736, 34, doi: 10.1088/0004-637X/736/1/34

Birnstiel, T., Fang, M., & Johansen, A. 2016, SSRv, 205, 41, doi: 10.1007/s11214-016-0256-1

Blum, J., & Münch, M. 1993, Icarus, 106, 151, doi: 10.1006/icar.1993.1163

Chambers, J. E., & Wetherill, G. W. 1998, Icarus, 136, 304, doi: 10.1006/icar.1998.6007

—. 2001, M&PS, 36, 381, doi: 10.1111/j.1945-5100.2001.tb01881.x

Childs, A. C., & Steffen, J. H. 2022, MNRAS, 511, 1848, doi: 10.1093/mnras/stac158

Clement, M. S., Kaib, N. A., & Chambers, J. E. 2020, PSJ, 1, 18, doi: 10.3847/PSJ/ab91aa

Colwell, J. E. 2003, Icarus, 164, 188, doi: 10.1016/S0019-1035(03)00083-6

Fabrycky, D. C., Lissauer, J. J., Ragozzine, D., et al. 2014, ApJ, 790, 146, doi: 10.1088/0004-637X/790/2/146

Hansen, B. M. S., & Murray, N. 2012, ApJ, 751, 158, doi: 10.1088/0004-637X/751/2/158

Hayashi, C. 1981, Progress of Theoretical Physics Supplement, 70, 35, doi: 10.1143/PTPS.70.35

Ida, S. 1990, Icarus, 88, 129, doi: 10.1016/0019-1035(90)90182-9

Ida, S., Canup, R. M., & Stewart, G. R. 1997, Nature, 389, 353, doi: 10.1038/38669

16

Ida, S., Kokubo, E., & Makino, J. 1993, MNRAS, 263, 875, doi: 10.1093/mnras/263.4.875

Ida, S., & Makino, J. 1993, Icarus, 106, 210, doi: 10.1006/icar.1993.1167

Ida, S., Ueta, S., Sasaki, T., & Ishizawa, Y. 2020, Nature Astronomy, 4, 880, doi: 10.1038/s41550-020-1049-8

Jetley, P., Gioachin, F., Mendes, C. Kale, L., & Quinn, T. 2008, Proceedings of IEEE International Parallel and Distributed Processing Symposium

Johansen, A., Blum, J., Tanaka, H., et al. 2014, in Protostars and Planets VI, ed. H. Beuther, R. S. Klessen, C. P. Dullemond, & T. Henning, 547

Johansen, A., Oishi, J. S., Mac Low, M.-M., et al. 2007, Nature, 448, 1022, doi: 10.1038/nature06086

Kokubo, E., & Ida, S. 1996, Icarus, 123, 180, doi: 10.1006/icar.1996.0148

—. 1998, Icarus, 131, 171, doi: 10.1006/icar.1997.5840

—. 2000, Icarus, 143, 15, doi: 10.1006/icar.1999.6237

—. 2002, ApJ, 581, 666, doi: 10.1086/344105

Leinhardt, Z. M., & Stewart, S. T. 2012, ApJ, 745, 79, doi: 10.1088/0004-637X/745/1/79

Lissauer, J. J., & Stewart, G. R. 1993, in Protostars and Planets III, ed. E. H. Levy & J. I. Lunine, 1061

Lyra, W., Johansen, A., Klahr, H., & Piskunov, N. 2008, A&A, 491, L41, doi: 10.1051/0004-6361:200810626

Menon, H., Wesolowski, L., & Zheng, G. e. a. 2015, Computational Astrophysics and Cosmology, 2, 1

Morishima, R., Stadel, J., & Moore, B. 2010, Icarus, 207, 517, doi: 10.1016/j.icarus.2009.11.038

Nakagawa, Y., Sekiya, M., & Hayashi, C. 1986, Icarus, 67, 375, doi: 10.1016/0019-1035(86)90121-1

Raymond, S. N., O'Brien, D. P., Morbidelli, A., & Kaib, N. A. 2009, Icarus, 203, 644, doi: 10.1016/j.icarus.2009.05.016

Raymond, S. N., Quinn, T., & Lunine, J. I. 2005, ApJ, 632, 670, doi: 10.1086/433179

—. 2006, Icarus, 183, 265, doi: 10.1016/j.icarus.2006.03.011

Raymond, S. N., Scalo, J., & Meadows, V. S. 2007, ApJ, 669, 606, doi: 10.1086/521587

Richardson, D. C. 1994, MNRAS, 269, 493, doi: 10.1093/mnras/269.2.493

Richardson, D. C., Quinn, T., Stadel, J., & Lake, G. 2000, Icarus, 143, 45, doi: 10.1006/icar.1999.6243

Safronov, V. S. 1969, Evoliutsiia doplanetnogo oblaka.

Wallace, S. C., & Quinn, T. R. 2019, MNRAS, 489, 2159, doi: 10.1093/mnras/stz2284

Weidenschilling, S. J. 1977, MNRAS, 180, 57, doi: 10.1093/mnras/180.2.57

—. 1989, Icarus, 80, 179, doi: 10.1016/0019-1035(89)90166-8

Wetherill, G. W., & Stewart, G. R. 1989, Icarus, 77, 330, doi: 10.1016/0019-1035(89)90093-6